JCIM JOURNAL OF CHEMICAL INFORMATION AND MODELING

pubs.acs.org/jcim Article

Stable Cavitation Interferes with $A\beta_{16-22}$ Oligomerization

Viet Hoang Man,* Xibing He, and Junmei Wang*

Cite This: J. Chem. Inf. Model. 2022, 62, 3885−3895 Read Online

ACCESS | Metrics & More | Article Recommendations | Supporting Information

ABSTRACT: Ultrasound and microbubbles are used for many medical applications nowadays. Scanning ultrasound can remove amyloid-β (Aβ) aggregates in the mouse brain and restores memory in an Alzheimer's disease mouse model. *In vitro* studies showed that amyloid fibrils are fragmented due to the ultrasound-induced bubble inertial cavitation, and ultrasonic pulses accelerate the depolymerization of Aβ fibrils into monomers at 1 μM of concentration. Under applied ultrasound, microbubbles can be in a stable oscillating state or unstable inertial cavitation state. The latter occurs when ultrasound causes a dramatic change of bubble sizes above a certain acoustic pressure. We have developed and implemented a nonequilibrium molecular dynamics simulation algorithm to the AMBER package, to facilitate the investigation of the molecular mechanism of Aβ oligomerization under stable cavitation. Our results indicated that stable cavitation not only inhibited oligomeric formation, but also prevented the formation of β-rich oligomers. The network analysis of state transitions revealed that stable cavitation altered the oligomerization pathways of $A\beta_{16-22}$ peptides. Our simulation tool may be applied to optimize the experimental conditions to achieve the best therapeutical effect.

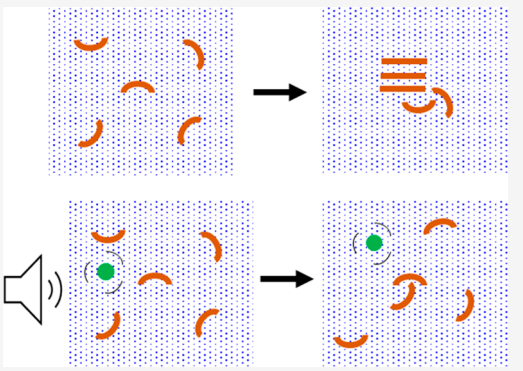

1. INTRODUCTION

Amyloid aggregation plays a critical role in the pathology of several neurodegenerative disorders including Alzheimer's disease (AD), Parkinson's disease, and Huntington's disease.[1−4] The aggregation of amyloid-β (Aβ) peptides is a main cause of AD. Aβ aggregation produces soluble oligomers followed by insoluble fibrillar structures. Both Aβ oligomers and fibrils are toxic to human cells, and a body of evidence showed that the former is more toxic than the latter.[5−7] Aβ fibrils are a main component of amyloid plaques which together with neurofibrillary tangles of Tau protein disrupt both internal and external neuron function and lead to cell death. Aβ oligomers are products of early Aβ aggregation state, oligomerization. They even occur before the first appearance of the disease's symptom and instigate multiple facets of AD-neuropathology.[5] Therefore, AD therapies targeting amyloid aggregation, particularly oligomerization, is of great interest.[8,9] The most popular approach focusing on amyloid aggregation study is to find good inhibitors to interfere with the aggregation process. Numerous screenings have been performed for the discovery of Aβ aggregation inhibitors, and the promising compounds have been tested in AD treatment.[10−16] However, the screenings did not confirm whether an inhibitor could inhibit the amyloid oligomerization or not. Additionally, efficiently passing through blood brain barrier (BBB) is a grand challenge for the potential compounds to reach the site of action. Other approaches including ultrasound and infrared laser have been applied to clear toxic Aβ aggregates and have shown promising results.[17−20] However, it is still a long way to develop a practical therapy from these findings. As of today, there is still not any drug or physical therapies targeting amyloid oligomerization that are approved for AD treatment.

Ultrasound has many medical applications including diagnosis, surgery, and therapy.[21] The possible side effects of therapeutic ultrasound, including bioeffects, hazards, and safety, also have been considered in numerous studies.[22] Recently, focused ultrasound (FUS) was proposed as a novel noninvasive therapeutic approach for AD.[23] The application of FUS in AD treatment can be classified into three catalogs: FUS stimulation, FUS coupled with microbubbles (FUS-MB) for drug delivery, and FUS-MB alone. FUS stimulation uses low intensity pulsed ultrasound with 1−2 MHz of frequency transducers to target the whole brain, hemisphere, or the hippocampus. It could decrease the expression of Aβ peptide, increase cholinergic activity and expression of neurotrophic factors, resulting in improvements in cognitive function and memory in preclinical models of AD.[24,25] FUS-MB uses low intensity ultrasounds (with 0.5−1.7 MHz of frequency transducers and the acoustic pressure of 0.3−0.67 MPa) and microbubble (MB) to open the BBB, and facilitate the permeation of various large therapeutic agents into the

Received: June 16, 2022
Published: August 3, 2022

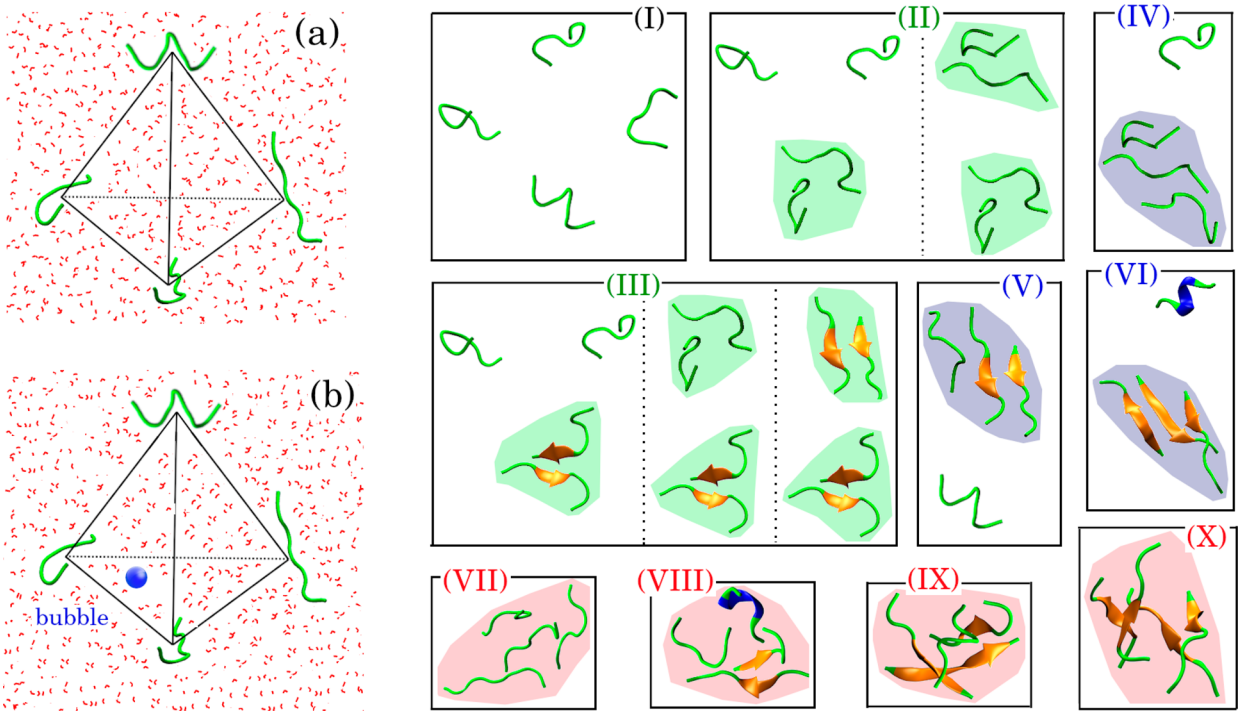

Figure 1. Setup of the control (a) and bubble-induced (b) systems, and the cartoon representation of 10 states formed by four Aβ_{16-22} peptides (right panel).

brain.[26−28] On the other hand, FUS-MB induced BBB opening alone could reduce the Aβ and Tau burden, enhance cholinergic function and induce neurogenesis.[29−31] Therefore, it can improve cognitive and memory deficits. However, ultrasound also showed different effects on amyloid aggregation in *in vitro* experiments. It was reported that ultrasound can accelerate the fibrillar formation of β_2-microglobulin, prion protein, and Aβ peptide.[32−34] On the other hand, it can also fragment Aβ fibrils into smaller fibrils and accelerate the depolymerization of fibrils into monomers at 1 μM concentration.[34,35] Thus, there is an urgent need to understand the mechanisms beyond those observations, and then optimize practical guidance on using therapeutic ultrasound in AD treatment.

In FUS-MB application, when ultrasound is applied, microbubbles start oscillating at the ultrasound frequency. A bubble can be in a stable vibrating state (stable cavitation), or unstable (inertial cavitation) if the ultrasound causes an acoustic pressure above a threshold. It is a challenge to gain insight on the mechanism of inertial and stable cavitations by experimental means due to the tiny size and fragility of bubbles. In complement to experiment, molecular dynamics (MD) simulation allows us to investigate microscopic structures and dynamics with fine time and size resolutions. Different models have been proposed to study bubble nucleation and inertial cavitation,[36−39] while only one method recently developed by us allows simulating the stable bubble cavitation.[18] In our method, a bubble is represented by a neutral particle with a small mass. The oscillation of the bubble which elicits the time-dependent Lennard-Jones interaction between the bubble and surrounding atoms is achieved by periodically changing the size of the bubble. We have implemented our bubble model into the GROMACS software package[40] and applied for all-atom MD simulation studies.[18,41] In this work, we advance the bubble model and implement it into the AMBER software package.[42] We applied the new function to study the effect of stable cavitation on Aβ_{16-22} oligomerization for the first time.

2. METHODOLOGY

2.1. Bubble Model and Implementation in AMBER.

The bubble model was implemented in GROMACS[40] for all-atom MD simulations in our previous studies.[18,41] In our method, a bubble is modeled by a particle with a small mass (m_{bb}) and without any charge. The bubble interacts with the surrounding atoms (waters and proteins) by a time-dependent Lennard-Jones potential as described by the following equation:

$$V[r, \sigma(t)] = c_0\left[\left(\frac{\sigma(t)}{r}\right)^{12} - \left(\frac{\sigma(t)}{r}\right)^{6}\right] \quad (1)$$

where r is the distance between the center of the bubble and the atoms of other molecules, and c_0 is a force constant which is related to the depth of the potential well. This potential prevents other molecules from approaching the particle, creating an empty spherical space which mimics a bubble with a radius $R(t) = \sigma(t)$. In this implementation, we controlled the activation of bubbles using parameter *ivjbmod*. If *ivjbmod* = 1 the bubbles are active (on), and if *ivjbmod* = 0 the bubbles are inactive (off). For multiple purposes of bubble simulation, we defined four bubble types. For bubble type 1, the center of the bubble is represented by a particle, and the bubble size oscillates according to eq 2. For bubble type 2, the center of the bubble is represented by a particle, and the size of bubbles takes different values for different time ranges of MD simulation as the following sequence: in the time-range of 0 → t_1, the bubble size is kept as R_{min}; in the second time-range, t_1 → t_2, the size of the bubble linearly increases from R_{min} to R_{max}; and in the last time-range, t_2 → the end of simulation, the

https://doi.org/10.1021/acs.jcim.2c00764
J. Chem. Inf. Model. 2022, 62, 3885−3895

bubble size is kept as R_{max}. Bubble types 3 and 4 are virtual bubbles, and the bubble position is the center of three selected atoms of the simulation system. The size of bubble type 3 is controlled with the same function being applied to bubble type 1, and the size of bubble type 4 is controlled with the same function being applied to bubble type 2. In this study, we studied Aβ_{16-22} oligomerization using bubble type 1 (the oscillation mode), in which the stable expansion and contraction of the bubble is mimicked by a harmonic vibration equation of the time-dependent bubble radius described by eq 2:

$$R(t) = \frac{R_{max} + R_{min}}{2} - \frac{R_{max} - R_{min}}{2}\cos(\omega(t - t_0)) \quad (2)$$

where R_{max} and R_{min} are maximum and minimum size of the bubble, respectively. t_0 is the initial time of the bubble simulation. The amplitude of the bubble varies between R_{max} and R_{min} with the vibrational frequency $f = 1/\tau = \omega/2\pi$. It is pointed out that only bubble type 1 was implemented in the GROMACS package, and all bubbles used the same set of parameters, $\{R_{max}, R_{min}, c_0, t_0, \omega\}$. In this new implementation into AMBER20, the size of each bubble is individually controlled by a set of parameters, $\{R_{max}, R_{min}, c_0, t_0, \omega, m_{bb}\}$, which are read from an input file. To study the effect of ultrasound on Aβ_{16-22} oligomerization, we applied the following parameters, R_{max} = 0.6 nm, R_{min} = 0.2 nm, τ = 50 ps and t_0 = 0 ps, for the oscillation bubble type 1. For bubble types 2 and 4, t_1 and t_2 correspond to t_0 and τ of the oscillation mode, respectively. More details and control parameters of the bubble model were described in the Supporting Information.

2.2. System Setup. To study the oligomerization of Aβ_{16-22} (ACE-KLVFFAE-NME) peptides, we first placed four Aβ_{16-22} monomers at the four vertices of a regular tetrahedron with the side length of 3.5 nm. The minimum distance between any two peptides is larger than 2 nm. The four-peptides then were put at the center of a truncated octahedral box, which has the volume of 409 nm^3 and was solvated by about 12255 water molecules (Figure 1a). The peptide concentration is around 16.2 mM. A certain number of Cl^- and Na^+ ions were added into the system so that the NaCl concentration is about 0.15 M. We used the four-peptide system to study the oligomerization which can form dimeric, trimeric, and tetrameric oligomers. Note that the tetramer was believed to be the most toxic Aβ oligomer.[43,44] Other benefits of applying the four-peptide system include the system is suitable for carrying out large-scale simulations, and by placing the four peptides at the vertices of a tetrahedron, a homogeneous system can be generated in a truncated octahedral box when applying the periodic boundary condition for MD simulations. For the purpose of sampling, we constructed 100 different four-peptide conformations and used as the initial structures for 100 independent MD runs. Note that the four monomers of a four-peptide structure were randomly selected from a monomeric databank containing 5000 Aβ_{16-22} monomers. To obtain the monomeric databank, we carried out a 100 ns NPT MD simulation of a monomer in explicit solvent and collected the 5000 monomeric structures from the last 50 ns to generate the databank. A four-peptide system with the presence of bubbles was built by randomly placing a bubble into the aforementioned four-peptide system (Figure 1). We named a system with presence of a bubble as a bubble-induced system and the one without bubble as a control system.

2.3. Molecular Dynamics Simulation Setting. All the molecular dynamics simulations were carried out using the pmemd.cuda module of the AMBER20 software package.[42] The ff14SB force field[45] and TIP3P water model[46] were adopted to model protein and the explicit solvent, respectively. The periodic boundary condition was applied for all simulations. The long-range Coulomb interaction was evaluated by the Particle-Mesh Ewald (PME) method,[47] with a cutoff of 1.0 nm for the direct calculation and reciprocal summation. The van der Waals interactions were calculated using atom-based nonbonded lists, and utilized a scheme to correct the long-range interactions beyond the cutoff of 1.0 nm. The constant pressure simulations were carried out at 1 atm via the Berendsen barostat[48] with the pressure relaxation time of 3.0 ps. Each system underwent the following sequential steps. First, the steepest descent minimization followed by a conjugate gradient minimization with the peptide atoms fixed at their initial positions, then the unrestrained steepest descent minimization followed by conjugate gradient minimization was carried out. The minimization steps were followed by a short MD simulation under constant volume while the system was heated from 0 to 310 K with weak restraints on the protein atoms. Next, Langevin dynamics at constant temperature (310 K) and constant pressure (1 atm) were carried out for 100 ps, and after that the density of the system was found to be stable around 1.0 g/cm^3. Finally, in the sampling phase, a 500 ns constant volume MD run at 310 K was performed using the leapfrog algorithm with a time step of 2 fs. The temperature was regulated using Langevin dynamics with a collision frequency of 1 ps^{-1}. The SHAKE algorithm[49] was applied to all bonds involving hydrogen atoms. Conformations were saved every 10 ps for postanalysis. In total, 50 000 snapshots were saved from each MD trajectory.

2.4. Data Analysis. *Basic Structural Parameters.* The secondary structure contents were classified into β, helix, and random coil using the STRIDE algorithm.[50,51] Here, the helix content includes 3−10 helix, π-helix, and α-helix, the β one consists of extended residues, and the rest is random coil. The CPPTRAJ module[52] was used to calculate the solvent accessible surface area (SASA), radius of gyration (R_g), and distances of interest. An intermolecular residue−residue interaction map was constructed using a 0.45 nm cutoff for the distance between a residue pair.

Free Energy Landscape (FEL). The free-energy surface along the N-dimensional reaction coordination $V_{1,2,3,...N}$ is given by $\Delta G = -k_B T[\ln P(V) - \ln P_{max}]$, where $P(V)$ is the probability distribution described by the histogram representation of the MD data. P_{max}, the maximum of distribution, is subtracted to ensure that the free energy ΔG has a minimum value of 0. The k_B and T are Boltzmann constant and simulation temperature, respectively. In this study, we used sum of end-to-end distances (e2e) of the four peptides and sum of distances between center of mass of any peptide pair (c2c) as reaction coordinates for the two-dimensional FEL.

Oligomerization Pathway Analysis. In the oligomerization of short Aβ peptides, the peptides first aggregate into oligomers; subsequently, the peptides of the oligomers are rearranged to form β-sheet structures. An oligomer can be characterized by oligomeric size (the number of peptides in an oligomer) and β-sheet size (the number of peptides forming β-sheets inside an oligomer). To investigate the oligomerization

https://doi.org/10.1021/acs.jcim.2c00764
J. Chem. Inf. Model. 2022, 62, 3885−3895

pathway of Aβ_{16-22} peptides, we classified the states of the four Aβ_{16-22} peptides into 10 classes based on the oligomeric and β-sheet formation of the peptides (Figure 1). The oligomers were formed if at least two peptides are in contact in space. Two peptides are in contact if their distance is smaller than or equal to 0.3 nm. A dimeric oligomer is formed when two monomers are in contact state. Three monomers would be a trimeric oligomer when a dimer is formed and at least one peptide of the dimer is in "contact state" with the third monomer. A tetrameric oligomer would be established when a trimeric oligomer is formed and at least one peptide of the trimer is in "contact state" with the fourth monomer. The four Aβ_{16-22} peptides are in one of the 10 states. In state I, the four peptides do not contact with each other, and there is not any oligomer in this state. In state II, there are only dimeric oligomers formed but without β-sheet formation. In state III, the largest oligomer is a dimer, and there is at least one dimer having a β-sheet structure formed. In state IV, a trimeric oligomer is formed but without β-sheet formation. In state V, there is a trimeric oligomer formed with two peptides forming a β-strand structure. State VI contains a trimeric oligomer with all the three peptides forming a β-strand structure. In the states VII, VIII, IX, and X, the four peptides formed a tetrameric oligomer, accompanied by the different numbers of β-strands formed.

3. RESULTS AND DISCUSSION

Convergence of conformational sampling is an important requirement for an amyloid aggregation study using MD simulations. To satisfy this requirement, one can use an enhanced conformational sampling technique, such as replica exchange MD or simulated tempering.[53,54] However, these techniques do not allow for tracking the evolution of the aggregation process directly. Thus, the aggregation pathways and kinetics, which are very important features of amyloid aggregation, cannot be obtained. On the other hand, conventional MD simulation allows us to easily track these aggregation characterizations. The limitation of the conventional MD simulation is that the system may be trapped in one of many local minima, leading to only a single pathway and the associated kinetics being observed, thus the aggregation picture is not fully described. To overcome this limitation, multiple long MD simulations starting from different initial structures should be used. We have applied this multiple MD simulation strategy in our previous amyloid aggregation studies, and have successfully obtained interesting and insightful results.[55−58] In this work, for each system, we sampled one hundred 500 ns MD simulation trajectories using different initial structures. Our simulations reached equilibrium states after 200 ns (Figure 2 and Figure S1). Therefore, most of the statistical analyses were performed using the data collected from the last 300 ns of an MD trajectory. The convergence of sampling is assessed by comparing the distributions of three reaction coordinates (intermolecular interaction energy (IIE), radius of gyration (R_g), and solvent accessible surface area (SASA)). The distributions of the three reaction coordinates were shown in Figure S2 for three ensemble statistics which were performed using the last 300 ns (from 200 to 500 ns) of all 100 trajectories, 220 ns spanning from 200 to 420 ns of all 100 trajectories, and the last 300 ns of 75 randomly selected trajectories, respectively. Obviously, the three ensemble statistics resulted in very similar distributions for all the three reaction coordinates. These results give us high confidence that our sampling strategy (100 independent 500 ns MD runs) can lead to sufficient and converged samplings, allowing us to discuss the impact of stable cavitation on the oligomerization of Aβ_{16-22} peptides.

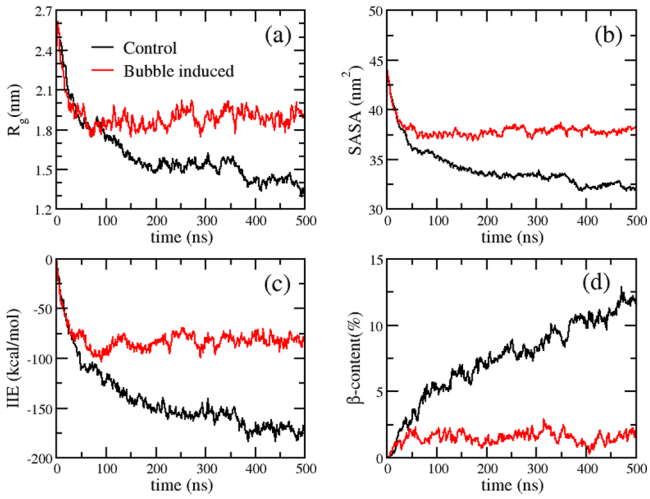

Figure 2. Evolution of R_g (a), SASA (b), IIE (c), and β-content (d) in control (black) and bubble-induced (red) systems. The data were averaged from 100 trajectories for each system.

3.1. Bubble Stable Cavitation Inhibits Aβ_{16-22} Oligomerization. To assess the oligomerization of Aβ_{16-22} peptides with and without the presence of bubble stable cavitation, we first considered general structural parameters including R_g, SASA, secondary structure contents, intermolecular residue−residue contact, and IIE of Aβ_{16-22} peptides. The time dependence of R_g, SASA, IIE, and β-content of Aβ_{16-22} peptides in the two systems is shown in Figure 2, and the evolution of the number of intermolecular residue−residue in-contact interactions ($N_{res\text{-}res}$), helix content, turn content, and coil content is shown in Figure S1. As expected, those parameters dramatically changed in the first 50 ns of a MD simulation, and fluctuated around the equilibrium values in the last 300 ns. The time of the first Aβ_{16-22} dimeric, trimeric, and tetrameric formations was 2 ± 1, 10 ± 3, and 32 ± 7 ns for the control system, and 2 ± 1, 10 ± 3, and 28 ± 7 ns for the bubble-induced system. These results are consistent with our previous findings that Aβ peptide oligomerization happened fast at high concentrations.[59] The parameter averages in the last 300 ns were shown in Table 1. The values of SASA and R_g of Aβ_{16-22} peptides in the control system were 33 ± 2 nm^2 and 1.5 ± 0.2 nm, respectively, much smaller than the corresponding values of 38 ± 2 nm^2 and 1.9 ± 0.2 nm in the bubble-induced system. Similarly, the values of $N_{res\text{-}res}$ and IIE, 34 ± 5 and −162 ± 20 kcal/mol in the control system, were much larger than those for the bubble induced system, which are 16 ± 3 and −81 ± 11 kcal/mol, respectively. As $N_{res\text{-}res}$ is a measure of compactness of two peptides and a larger value implies that more residue pairs are in the contact state, the much larger $N_{res\text{-}res}$ value of the control system suggests that Aβ_{16-22} peptides form more compact structures in the control system than in the bubble induced system (Figure 3a). For the secondary structures, helix and turn contents were similar between the two systems, while the β content in the control system was five times higher than that in the bubble-induced system (Figure 2d). Nevertheless, the β propensity of each amino acid of Aβ_{16-22} peptides in the two

https://doi.org/10.1021/acs.jcim.2c00764
J. Chem. Inf. Model. 2022, 62, 3885−3895

Table 1. Averaged Values of the Overall Structural Parameters from the Last 300 ns of MD Simulations. The Errors Are Standard Deviation

system	β (%)	helix (%)	turn (%)	coil (%)	SASA (nm^2)	R_g(nM)	$N_{res\text{-}res}$	IIE(kcal/mol)
control	10 ± 3	9 ± 2	35 ± 3	46 ± 3	33 ± 2	1.5 ± 0.2	34 ± 5	−162 ± 20
bubble-induced	2 ± 2	7 ± 2	37 ± 3	54 ± 4	38 ± 2	1.9 ± 0.2	16 ± 3	−81 ± 11

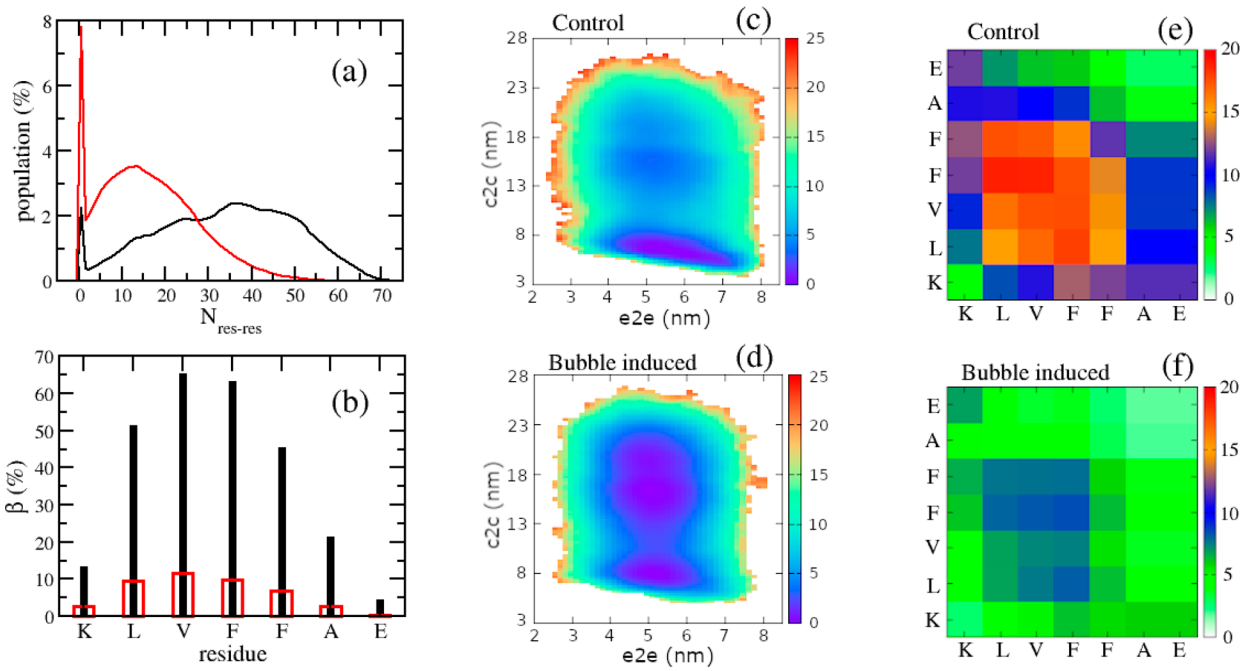

Figure 3. Population of $N_{res\text{-}res}$ (a), β propensity of residues (b), FELs (c and d), and intermolecular residue−residue interaction maps (e and f) in control and bubble-induced systems. In panels a and b, the data of control and bubble-induced systems were shown in black and red colors, respectively. The data were calculated from 100 trajectories for each system and the last 300 ns of each trajectory.

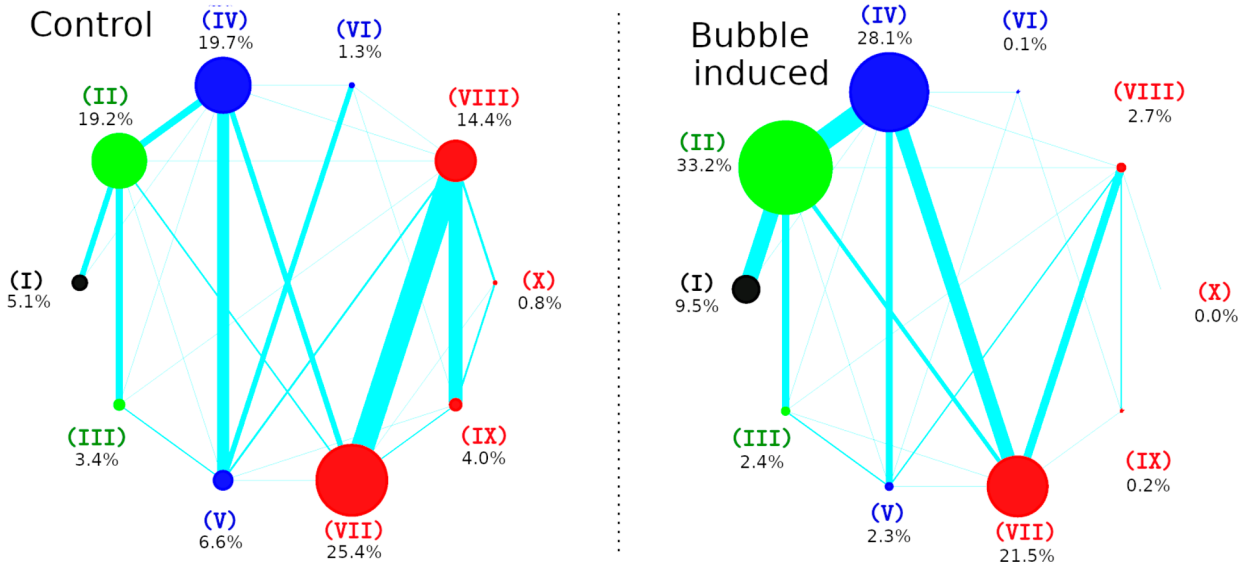

Figure 4. Population sizes of the 10 states and the transitions among the states in the different systems. The population of a state are proportional to the circle area representing the state, and the population values were also explicitly shown by black numbers. The transition frequency between two states was proportional to the width of the line linking the two states. The data were calculated from 100 trajectories for each system and the whole 500 ns of each trajectory.

systems followed a similar trend, which was V18 > F19 > L17 > F20 > A21 > K16 > E22 (Figure 3b).

Next, as shown in Figure 3c,d, we constructed free energy landscapes using two reaction coordinates, end-to-end (e2e) and center-to-center (c2c) distances. For a short Aβ peptide, the longer is its e2e distance, the easier it is for the peptide to form strand structure (in β-sheet). For an oligomer, the c2c distance is inversely proportional to the compactness. The

https://doi.org/10.1021/acs.jcim.2c00764
J. Chem. Inf. Model. 2022, 62, 3885−3895

FELs of both systems had three local minima. Thus, we performed k-mean clustering analysis on the FELs data to obtain the centers of the minima and population sizes. For the control system, the minima were located at (5.6, 7.0), (5.3, 14.1), and (5.1, 19.1) and the corresponding population sizes were 55%, 27%, and 18%. While for the bubble induced system, the minima were located at (5.1, 15.3), (5.1, 20.0), and (5.3, 8.9) with the corresponding population sizes of 38.9%, 31.4%, and 29.7%. Note that the location of a local minimum takes a format of (e2e, c2c). This result showed that the peptides are more extended in the control system than in the bubble induced system as the former has larger e2e values; and oligomers is more compact in the control system than in the bubble induced system as the former has smaller c2c values. We also constructed intermolecular residue−residue interaction maps shown in Figure 3e,f. The pattern of the two maps was similar to each other, and the interactions between L17, V18, F19, and F20 residues are stronger than the other residue pairs. However, as to an individual residue pair, the two residues in contact interaction occurs more frequently in the control system than in the bubble induced system. Those results suggested that bubble stable cavitation not only interferes with the Aβ_{16-22} oligomerization but also inhibits Aβ_{16-22} β-sheet formation.

3.2. Impact of the Bubble Stable Cavitation on the Aβ_{16-22} Oligomerization Pathways. In a self-assembly of Aβ peptides, the peptides aggregate into none-β-sheet oligomers in the early phase, then the oligomeric peptides rearrange to form β-sheet structures in the later phase. To depict the oligomerization pathways, we have defined 10 aggregation states formed by the four Aβ_{16-22} peptides (Figure 1). Note that, among the oligomeric states (II → X), II (dimer), IV (trimer), and VII (tetramer) states are none-β-sheet structural oligomers, while the other states are β structural oligomers. The population sizes of the 10 states and the transitions between the states in the two systems were shown in Figure 4, and were summarized for all MD snapshots collected from 100 MD trajectories for each system. Similar figures, but for individual trajectories, were shown in Figures S3 and S4. It was shown that the bubble stable cavitation had a strong impact on the oligomerization pathways as the population sizes and transitions were very different between the two systems. The population of monomeric state (I) was two times larger in the bubble induced system than in the control system, while the population of the largest oligomer, i.e., tetramer (VII, VIII, IX, and X states) was much higher in the control system than in the bubble-induced system. In other words, bubble stable cavitation inhibited oligomeric formation of Aβ_{16-22} peptides. For a given oligomer, the β/none-β sheet population ratios in the control system were much larger than that in the bubble-induced system. In the control system, the β/none-β sheet population ratios were 0.18 for dimer, 0.4 for trimer, and 0.76 for tetramer. While in the bubble-induced system, the ratios were 0.07, 0.08, and 0.13 for dimer, trimer and tetramer, respectively. It clearly showed that bubble stable cavitation interfered with the rearrangement of peptides in an oligomer into β-sheet structures. The transition frequency between two states was different from one state pair to another, and from one system to another. In the control system, the most occurring state transitions were from IV → V, VII → VII, and VIII → IX, which are from none-β sheet to β-sheet oligomeric transitions. While in the bubble induced system, the most occurring state transitions were from I → II, II → IV, and IV → VII, which are none-β sheet to none-β sheet transitions. This result pointed out that during 500 ns of simulation, the early phase of the Aβ_{16-22} oligomerization in the control system was short, and the peptides spent much more time on the later phase. In contrast, in the bubble-induced system, the peptides spent much more time on the early phase, and the none-β sheet oligomers were unstable and easily broken into monomer and smaller oligomers. The 10 oligomeric states were further characterized by the reaction coordinates including SASA, $N_{res-res}$, potential energy, and IIE. As shown in Figure 5, for the same state from II to X, the

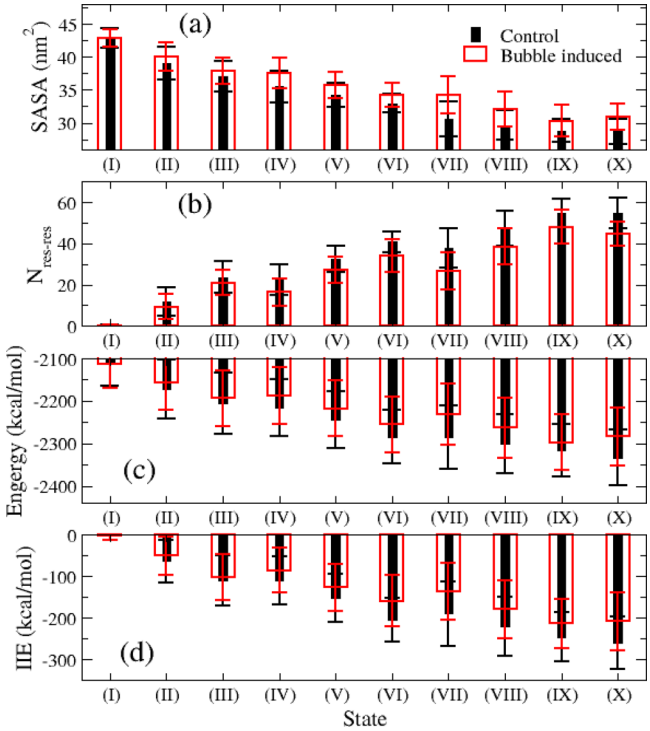

Figure 5. Characterizations of the 10 states in control (black) and bubble-induced (red) systems. The errors are standard deviation. The data were calculated from 100 trajectories for each system and the whole 500 ns of each trajectory.

oligomers in the bubble induced system have higher potential energy and IIE, larger SASA, and smaller $N_{res-res}$ than the corresponding ones of oligomers in the control system. Those data suggested that the oligomers formed in the control system are more stable than the oligomers in the bubble-induced system.

There are many oligomerization pathways for peptides to go from state I to state X, which are constructed by the combination of the following transitions, I → II, II → III, II → IV, II → VII, III → V, IV → V, IV → VII, V → VI, V → VIII, VI → IX, VII → VIII, VII → IX, VIII → IX, VIII → X, and IX → X. The probability of a transition between two states depends on the potential energy difference of the two states. The probability of the transition from State i to State j can be estimated by the following equation: $P_{ij} = \min\{1, e^{-\Delta E_{ij}/k_bT}\}$, where $\Delta E_{ij} = E_j - E_i$. If E_j is lower than E_i, the $P_{ij} \sim 1$. If E_j is higher than E_i, then $P_{ij} = e^{-\Delta E_{ij}/k_bT}$. Therefore, the smaller $|\Delta E_{ij}|$ is, the higher is the probability of the transition from a low energy state to a high energy state. Therefore, the frequency of i and j state transition is proportional to $|\Delta E_{ij}|$. This can be applied to explain the difference of the state transitions as well

https://doi.org/10.1021/acs.jcim.2c00764
J. Chem. Inf. Model. 2022, 62, 3885−3895

as oligomerization pathways of the $A\beta_{16-22}$ peptides in the two system. For example, the $|\Delta E_{ij}|$ of I → II, II → IV, and IV → VII state pairs were 42.8, 74.5, and 118.3 kcal/mol in the bubble-induced system, which are smaller than the corresponding $|\Delta E_{ij}|$ in the control system, which were 60.8, 104.5, and 175.2 kcal/mol, respectively. As such, the frequencies of I → II, II → IV, and IV → VII state transitions in the bubble induced system were higher than the ones in the control system (Figure 5). In contrast, for the cases of IV → V, VII → VIII, and VIII → IX state transitions, the $|\Delta E_{ij}|$ in the control system (28.5, 14.9, and 26 kcal/mol) were smaller than the $|\Delta E_{ij}|$ in the bubble induced system (29.8, 30.5, and 35.3 kcal/mol). Therefore, the frequencies of IV → V, VII → VIII, and VIII → IX state transitions in the control system were higher than in the bubble induced system (Figure 4).

Ohhashi et al. showed that the fibril formation of β_2-microglobulin was accelerated by ultrasound, because the ultrasound can induce amyloid nucleation.[32] The concentration of β_2-microglobulin monomer was 25 μM in the experiment of Ohhashi et al. As for Aβ peptide, Yagi et al. pointed out that ultrasonic pulses accelerated spontaneous fibrillation when the peptide concentration was above 1 μM, while it also accelerated the depolymerization of fibrils into monomers at or below 1 μM.[34] The results of Yagi et al. indicated ultrasound can inhibit Aβ aggregation at low monomeric concentrations of Aβ peptides. On the other side, FUS stimulation and FUS-MB treatment provided positive results as they can increase cholinergic activity and expression of neurotrophic factors.[23−26,29−31] Particularly, FUS-MB treatment could reduce Aβ and Tau burden in the brain of AD rodent model.[29−31,60] Poon et al. found that single FUS-MB treatment significantly reduced Aβ plaque volume at 2 days postsonication. Lee et al. showed that repeated FUS-MB treatments reduced Aβ deposits in the entire brain as well as targeted regions, increased solute Aβ to the CSF space, and enhanced CSF Aβ drainage. Although some different mechanisms of the therapeutic effects have been proposed,[29−31,60] these results also implied that ultrasound, especially stable cavitation, could interfere with the aggregation of Aβ peptides in the brain, in which the peptide concentration is in the nanomolar range. To our best knowledge, no study that considers the effect of stable cavitation on amyloid oligomerization has been performed yet.

To observe the stable cavitation in a reasonable simulation time scale, we used the bubble with the equilibrium radius of 0.4 nm, and the vibrational frequency of 20 GHz (τ = 0.05 ns). These values are different from those in FUS-MB studies: a microbubble has the radii ranging from 0.5 to 4 μm, and ultrasound frequency is from 0.5 to 2 MHz (τ in range of 2000−500 ns). We acknowledge that current computer power does not allow us to perform all-atom simulations at the microsecond time scale to simulate at least several ultrasound cycles with at least one real bubble inside of a large simulation box with a size of several micrometers. Nevertheless, despite the significant difference between our parameters and experiments, our previous study showed that the mechanism should be the same in the case that the bubble cavitation exerts shear stress on surrounding objects.[18] Also the Rayleigh-Plesset equation,[61−63] which was derived from the first-principles to describe the bubble cavitation in liquids in terms of macroscopic hydrodynamics, still well describes the dynamics of sub-nanobubbles in terms of inertia, surface tension, and viscosity.[41] Therefore, our bubble model should be sufficiently accurate to represent stable cavitations in experiment. On the other side, assuming the Aβ concentration (C_p) in the FUS-MB experiment is about 100 nM (Aβ concentration in the brain is approximately in nM range) and the ultrasound frequency (f_{US}) is 1 MHz, we obtain the ratio $f_{US}/C_P \approx 10^7$ Hz/μM for the FUS-MB experiment. Yagi et al. found with their *in vitro* experiment that 20 kHz-ultrasound can actually inhibit Aβ aggregation at an Aβ concentration equal to or lower than 1 μM.[34] The calculated ratio f_{US}/C_P is greater than 2×10^4 Hz/μM for ultrasounds to be inhibitive. From these results, we hypothesized that ultrasounds can inhibit Aβ aggregation if the ratio f_{US}/C_P is greater than 2×10^4 Hz/μM. In our bubble simulation, our stable cavitation has 20 GHz of vibration frequency, and the concentration of Aβ peptide was 16.2 mM. The calculated ratio f_{US}/C_P is about 10^6 Hz/μM, which is significantly greater than 2×10^4 Hz/μM for our simulation setting. Thus, for the practice in investigating the impact of stable cavitation on Aβ oligomerization with available computational resources, our simulation parameters including bubble size, ultrasound frequency, and Aβ concentration are reasonable and sufficient for this proof-of-concept study. Of course, our finding will need confirmations by future experiment. Next, we will find the correspondence between the simulation parameters and FUS experimental parameters, to pave the road of applying molecular simulations to optimize the FUS-MB experimental protocol.

3.3. Applications of Bubble Simulation. Microbubbles and nanobubbles have small size and many special characteristics such as high bioactivity, low rising velocity, decreased friction drags, high internal pressure, large gas dissolution capacity, and ability to be crushed and to form free radicals.[64] They have wide applications in many fields such as engineering, agriculture, environment, and food, particularly biomedical diagnosis and therapy.[64] In medicine, microbubbles and nanobubbles have shown a great potential for the growth of applications in drug delivery, systemic gene delivery, theranostic oncology, and the treatments of ocular diseases and dementia.[26,27,65−69] Understanding the underlying mechanisms of effects and interactions of the bubbles to biological agents is of a great interest, since it can facilitate to not only improve and optimize the protocols of the existing applications, but also expand the application domains. However, this task is a challenge in experiment due to the tiny size and fragility of the bubbles. Fortunately, computational approaches such as MD simulation which is complement to experiment can gain insight into the mechanisms.

Many bubble simulations have been carried out to study inertial cavitations, in which the bubbles were modeled by empty spheres.[70−76] However, these empty bubble models have the following limitations. First, the bubbles are not stable and will collapse in a short time of equilibrium simulation. Second, researchers need a good programing/coding skill to design study systems since they need to write their own code to remove waters in the bubble space and modify topology files accordingly to run simulations. Finally, these empty bubble models cannot be used to represent stable cavitations, which participate in many biological phenomena with ultrasound. In contrast, our newly developed bubble model can simulate stable cavitation with easy system setup and no need to modify topology files. Before this work, we had applied bubble simulation of stable cavitation (using bubble type 1) to investigate the dissociation of amyloid fibrils by bubble cavitation, the molecular mechanism of the cell membrane

https://doi.org/10.1021/acs.jcim.2c00764
J. Chem. Inf. Model. 2022, 62, 3885−3895

pore formation induced by bubble stable cavitation.[18,77,78] Another possible application of bubble types 1 or 3 simulation is to study the effect of stable cavitation on ion channel, which is one of the mechanisms of focused ultrasound for neuromodulation,[79] as shown in Figure S5. The simulation using our bubble types 2 or 4 can create empty bubbles that are used to model inertial cavitations. For this application, one would first run simulations using bubble type 2 or 4 to create a bubble of a given bubble size, then the simulation would continued with the bubble mode being turned off to study inertial cavitation.

Although bubble simulation has a broad range of applications that are complementary to experimental studies, it also has limitations due to the significant differences of parameter/condition settings between simulation and experiment. Therefore, designing a system and choosing suitable parameters of simulation for a given study purpose should be seriously taken into account. For example, in this work, we performed bubble simulation to resemble a FUS-MB experiment which can reduce the deposit of Aβ aggregates in the targeted regions of the brain. We designed four-peptide systems with and without the presence of stable cavitation. This system design not only allows us performing large-scale simulation, but also is suitable to investigate the oligomerization of Aβ peptides. Additionally, bubble vibrational frequency and Aβ concentration in our bubble simulation had a suitable f_{US}/C_P ratio, at which stable cavitation can inhibit Aβ aggregation based on experimental indication. Moreover, these simulation parameters, peptide concentration, and bubble vibrational frequency, allowed us to perform the study with a reasonable computational resource.

On the other hand, we carried out NVT (constant number of particles, volume, and temperature) instead of NPT (constant number of particles, pressure, and temperature) simulation since the latter one may interfere with the effect of ultrasound at the time the pressure was coupled. However, NPT simulation for stable cavitation still works if the time of pressure coupling is much greater than the period of the bubble vibration. Importantly, we used a small size of the bubble (0.4 nm) and amplitude of the bubble vibration (0.4 nm), resulting in a very small volume change between the maximum and minimum size of the bubble, 0.87 nm^3, which accounts for ∼0.2% of the system volume. Thus, our NVT bubble simulation can also avoid the artificial pressure caused by the change of bubble size.

4. CONCLUSIONS

We have advanced a bubble model and implemented it into the AMBER software package. Each bubble is controlled by its own parameter set to achieve stable cavitation in all-atom simulations. We utilized this new tool investigating the effect of stable cavitation on Aβ_{16-22} oligomerization. Our result showed that stable cavitation strongly interfered with the oligomerization and inhibited the β-sheet formation of Aβ16−22 peptides. This finding revealed the underlying mechanisms of FUS-MB therapies for AD treatment and facilitated researchers to establish experimental protocols through molecular simulations to effectively interfere with amyloid aggregation utilizing FUS-MB.

■ ASSOCIATED CONTENT

Supporting Information

The Supporting Information is available free of charge at https://pubs.acs.org/doi/10.1021/acs.jcim.2c00764.

Details on how to run bubble simulations in AMBER; evolution of $N_{res\text{-}res}$ and secondary structures; normalized distributions of IIE, R_g, and SASA; population of the 10 states and the transitions between those states in the control system and a bubble-induced system; design to study the impact of stable cavitation on ion channel (PDF)

■ AUTHOR INFORMATION

Corresponding Authors

Viet Hoang Man − *Department of Pharmaceutical Sciences and Computational Chemical Genomics Screening Center, School of Pharmacy, University of Pittsburgh, Pittsburgh, Pennsylvania 15261, United States;* orcid.org/0000-0002-8907-6479; Email: vhm3@pitt.edu

Junmei Wang − *Department of Pharmaceutical Sciences and Computational Chemical Genomics Screening Center, School of Pharmacy, University of Pittsburgh, Pittsburgh, Pennsylvania 15261, United States;* orcid.org/0000-0002-9607-8229; Email: junmei.wang@pitt.edu

Author

Xibing He − *Department of Pharmaceutical Sciences and Computational Chemical Genomics Screening Center, School of Pharmacy, University of Pittsburgh, Pittsburgh, Pennsylvania 15261, United States;* orcid.org/0000-0001-7431-7893

Complete contact information is available at: https://pubs.acs.org/10.1021/acs.jcim.2c00764

Author Contributions

V.H.M. and J.W. designed the experiment; V.H.M. performed simulations and data analysis. V.H.M., X.B., and J.W. discussed and wrote the paper.

Notes

The authors declare no competing financial interest.

Data and Software Availability. All the data were collected by running MD simulations with the AMBER software package. The function of bubble simulations has been implemented in AMBER 22.

■ ACKNOWLEDGMENTS

This work was supported by the funds from the National Institutes of Health (NIH) NIH R01GM079383, NIH K25AG070277, and the National Science Foundation (NSF) 1955260. The authors thank the computing resources provided by the Center for Research Computing (CRC) at University of Pittsburgh.

■ REFERENCES

(1) Hardy, J.; Selkoe, D. J. The Amyloid Hypothesis of Alzheimer's Disease: Progress and Problems on the Road to Therapeutics. *Science* **2002**, *297*, 353−356.

(2) Polymeropoulos, M. H.; Lavedan, C.; Leroy, E.; Ide, S. E.; Dehejia, A.; Dutra, A.; Pike, B.; Root, H.; Rubenstein, J.; Boyer, R.; Stenroos, E. S.; Chandrasekharappa, S.; Athanassiadou, A.; Papapetropoulos, T.; Johnson, W. G.; Lazzarini, A. M.; Duvoisin, R. C.; Di Iorio, G.; Golbe, L. I.; Nussbaum, R. L. Mutation in the α-

synuclein Gene Identified in Families with Parkinson's Disease. *Science* **1997**, *276*, 2045−2047.
(3) Singleton, A. B.; Farrer, M.; Johnson, J.; Singleton, A.; Hague, S.; Kachergus, J.; Hulihan, M.; Peuralinna, T.; Dutra, A.; Nussbaum, R.; Lincoln, S.; Crawley, A.; Hanson, M.; Maraganore, D.; Adler, C.; Cookson, M. R.; Muenter, M.; Baptista, M.; Miller, D.; Blancato, J.; Hardy, J.; Gwinn-Hardy, K. Alpha-Synuclein Locus Triplication Causes Parkinson's Disease. *Science* **2003**, *302*, 841.
(4) Urbanc, B. Cross-Linked Amyloid β-Protein Oligomers: A Missing Link in Alzheimer's Disease Pathology? *J. Phys. Chem. B* **2021**, *125*, 1307−1316.
(5) Cline, E. N.; Bicca, M. A.; Viola, K. L.; Klein, W. L. The Amyloid-β Oligomer Hypothesis: Beginning of the Third Decade. *J. Alzheimers Dis.* **2018**, *64*, S567−S610.
(6) Hayden, E. Y.; Teplow, D. B. Amyloid β-protein Oligomers and Alzheimer's Disease. *Alzheimers Res. Ther.* **2013**, *5*, 60.
(7) Sengupta, U.; Nilson, A. N.; Kayed, R. The Role of Amyloid-β Oligomers in Toxicity, Propagation, and Immunotherapy. *EBioMedicine* **2016**, *6*, 42−49.
(8) Jeremic, D.; Jimenez-Diaz, L.; Navarro-Lopez, J. D. Past, Present and Future of Therapeutic Strategies Against Amyloid-β Peptides in Alzheimer's Disease: a Systematic Review. *Ageing Res. Rev.* **2021**, *72*, 101496.
(9) Leinenga, G.; Gotz, J. Scanning Ultrasound Removes Amyloid-β and Restores Memory in an Alzheimer's Disease Mouse Model. *Sci. Transl. Med.* **2015**, *7*, 278ra33.
(10) Das, S.; Smid, S. D. Identification of Dibenzyl Imidazolidine and Triazole Acetamide Derivatives Through Virtual Screening Targeting Amyloid-β Aggregation and Neurotoxicity in PC12 Cells. *Eur. J. Med. Chem.* **2017**, *130*, 354−364.
(11) Du, W. J.; Guo, J. J.; Gao, M. T.; Hu, S. Q.; Dong, X. Y.; Han, Y. F.; Liu, F. F.; Jiang, S. Y.; Sun, Y. Brazilin Inhibits Amyloid β-protein Fibrillogenesis, Remodels Amyloid Fibrils and Reduces Amyloid Cytotoxicity Functional. *Sci. Rep.* **2015**, *5*, 7992 DOI: 10.1038/srep07992.
(12) Lu, C. J.; Guo, Y. Y.; Yan, J.; Luo, Z. H.; Luo, H. B.; Yan, M.; Huang, L.; Li, X. S. Design, Synthesis, and Evaluation of Multitarget-Directed Resveratrol Derivatives for the Treatment of Alzheimer's Disease. *J. Med. Chem.* **2013**, *56*, 5843−5859.
(13) Rigi, G.; Nakhaei, M. V. A.; Eidipour, H.; Najimi, A.; Tajik, F.; Taher, N.; Yarahmadi, K. Virtual Screening Following Rational Drug Design Based Approach for Introducing new Anti Amyloid-β aggregation agent. *Bioinformation* **2017**, *13*, 42−45.
(14) Shytle, R. D.; Bickford, P. C.; Rezai-Zadeh, K.; Hou, L.; Zeng, J.; Tan, J.; Sanberg, P. R.; Sanberg, C. D.; Roschek, B.; Fink, R. C.; Alberte, R. S. Optimized Turmeric Extracts Have Potent Anti-Amyloidogenic Effects. *Curr. Alzheimer Res.* **2009**, *6*, 564−571.
(15) Viet, M. H.; Siposova, K.; Bednarikova, Z.; Antosova, A.; Nguyen, T. T.; Gazova, Z.; Li, M. S. In Silico and in Vitro Study of Binding Affinity of Tripeptides to Amyloid-β Fibrils: Implications for Alzheimer's Disease. *J. Phys. Chem. B* **2015**, *119*, 5145−5155.
(16) Zhao, J. H.; Liu, H. L.; Elumalai, P.; Chen, W. H.; Men, L. C.; Liu, K. T. Molecular Modeling to Investigate the Binding of Congo Red toward GNNQQNY Protofibril and In Silico Virtual Screening for the Identification of New Aggregation Inhibitors. *J. Mol. Model* **2013**, *19*, 151−162.
(17) Okumura, H.; Itoh, S. G. Amyloid Fibril Disruption by Ultrasonic Cavitation: Nonequilibrium Molecular Dynamics Simulations. *J. Am. Chem. Soc.* **2014**, *136*, 10549−10552.
(18) Hoang Viet, M.; Derreumaux, P.; Nguyen, P. H. Nonequilibrium All-atom Molecular Dynamics Simulation of the Bubble Cavitation and Application to Dissociate Amyloid Fibrils. *J. Chem. Phys.* **2016**, *145*, 174113.
(19) Hoang Viet, M.; Derreumaux, P.; Li, M. S.; Roland, C.; Sagui, C.; Nguyen, P. H. Picosecond Dissociation of Amyloid Fibrils with Infrared Laser: A Nonequilibrium Simulation Study. *J. Chem. Phys.* **2015**, *143*, 155101.
(20) Kawasaki, T.; Man, V. H.; Sugimoto, Y.; Sugiyama, N.; Yamamoto, H.; Tsukiyama, K.; Wang, J.; Derreumaux, P.; Nguyen, P. H. Infrared Laser-Induced Amyloid Fibril Dissociation: A Joint Experimental/Theoretical Study on the GNNQQNY Peptide. *J. Phys. Chem. B* **2020**, *124*, 6266−6277.
(21) Sarvazyan, A. P.; Rudenko, O. V.; Nyborg, W. L. Biomedical Applications of Radiation Force of Ultrasound: Historical Roots and Physical Basis. *Ultrasound Med. .Biol.* **2010**, *36*, 1379−1394.
(22) Izadifar, Z.; Babyn, P.; Chapman, D. Mechanical and Biological Effects of Ultrasound: A Review of Present Knowledge. *Ultrasound Med. Biol.* **2017**, *43*, 1085−1104.
(23) Liu, X.; Naomi, S. S. M.; Sharon, W. L.; Russell, E. J. The Applications of Focused Ultrasound (FUS) in Alzheimer's Disease Treatment: A Systematic Review on Both Animal and Human Studies. *Aging Dis* **2021**, *12*, 1977−2002.
(24) Lin, W. T.; Chen, R. C.; Lu, W. W.; Liu, S. H.; Yang, F. Y. Protective Effects of Low-intensity Pulsed Ultrasound on Aluminum-induced Cerebral Damage in Alzheimer's Disease Rat Model. *Sci. Rep.* **2015**, *5*, 9671.
(25) Eguchi, K.; Shindo, T.; Ito, K.; Ogata, T.; Kurosawa, R.; Kagaya, Y.; Monma, Y.; Ichijo, S.; Kasukabe, S.; Miyata, S.; Yoshikawa, T.; Yanai, K.; Taki, H.; Kanai, H.; Osumi, N.; Shimokawa, H. Whole-brain Low-intensity Pulsed Ultrasound Therapy Markedly Improves Cognitive Dysfunctions in Mouse Models of Dementia - Crucial Roles of Endothelial Nitric Oxide Synthase. *Brain Stimul.* **2018**, *11*, 959−973.
(26) Hsu, P. H.; Lin, Y. T.; Chung, Y. H.; Lin, K. J.; Yang, L. Y.; Yen, T. C.; Liu, H. L. Focused Ultrasound-Induced Blood-Brain Barrier Opening Enhances GSK-3 Inhibitor Delivery for Amyloid-Beta Plaque Reduction. *Sci. Rep.* **2018**, *8*, 12882.
(27) Liu, Y. A.; Gong, Y. C.; Xie, W. J.; Huang, A. L.; Yuan, X. Y.; Zhou, H.; Zhu, X. F.; Chen, X.; Liu, J. W.; Liu, J.; Qin, X. Y. Microbubbles in Combination with Focused Ultrasound for the Delivery of Quercetin-modified Sulfur Nanoparticles Through the Blood Brain Barrier into the Brain Parenchyma and Relief of Endoplasmic Reticulum Stress to Treat Alzheimer's Disease. *Nanoscale* **2020**, *12*, 6498−6511.
(28) Xhima, K.; Markham-Coultes, K.; Nedev, H.; Heinen, S.; Saragovi, H. U.; Hynynen, K.; Aubert, I. Focused Ultrasound Delivery of a Selective TrkA Agonist Rescues Cholinergic Function in a Mouse Model of Alzheimer's Disease. *Sci. Adv.* **2020**, *6*, eaax6646.
(29) Poon, C. T.; Shah, K.; Lin, C.; Tse, R.; Kim, K. K.; Mooney, S.; Aubert, I.; Stefanovic, B.; Hynynen, K. Time Course of Focused Ultrasound Effects on β-amyloid Plaque Pathology in the TgCRND8Mouse Model of Alzheimer's Disease. *Sci. Rep.* **2018**, *8*, 14061.
(30) Karakatsani, M. E.; Kugelman, T.; Ji, R.; Murillo, M.; Wang, S.; Niimi, Y.; Small, S. A.; Duff, K. E.; Konofagou, E. E. Unilateral Focused Ultrasound-Induced Blood-Brain Barrier Opening Reduces Phosphorylated Tau from The rTg4510 Mouse Model. *Theranostics* **2019**, *9*, 5396−5411.
(31) Shin, J.; Kong, C.; Lee, J.; Choi, B. Y.; Sim, J.; Koh, C. S.; Park, M.; Na, Y. C.; Suh, S. W.; Chang, W. S.; Chang, J. W. Focused Ultrasound-induced Blood-brain Barrier Opening Improves Adult Hippocampal Neurogenesis and Cognitive Function in a Cholinergic Degeneration Dementia Rat Model. *Alzheimers Res. Ther.* **2019**, *11*, 110.
(32) Ohhashi, Y.; Kihara, M.; Naiki, H.; Goto, Y. Ultrasonication-induced Amyloid Fibril Formation of β2-microglobulin. *J. Biol. Chem.* **2005**, *280*, 32843−32848.
(33) Yamaguchi, K. I.; Honda, R. P.; Elhelaly, A. E.; Kuwata, K. Acceleration of Nucleation of Prion Protein During Continuous Ultrasonication. *J. Biochem.* **2018**, *163*, 503−513.
(34) Yagi, H.; Hasegawa, K.; Yoshimura, Y.; Goto, Y. Acceleration of the Depolymerization of Amyloid-β Fibrils by Ultrasonication. *Biochim. Biophys. Acta* **2013**, *1834*, 2480−2485.
(35) Chatani, E.; Lee, Y. H.; Yagi, H.; Yoshimura, Y.; Naiki, H.; Goto, Y. Ultrasonication-Dependent Production and Breakdown Lead to Minimum-sized Amyloid Fibrils. *Proc. Natl. Acad. Sci. U.S.A.* **2009**, *106*, 11119−11124.

(36) Tsuda, S.-I.; Tokumasu, T.; Kamijo, K. A Molecular Dynamics Study of Bubble Nucleation in Liquid Oxygen with Impurities. *Heat Transfer* **2005**, *34*, 514−526.
(37) Wu, Y. W.; Pan, C. A Molecular Dynamics Simulation of Bubble Nucleation in Homogeneous Liquid under Heating with Constant Mean Negative Pressure. *Microscale Therm. Eng.* **2003**, *7*, 137−151.
(38) Zhai, M.; Zhang, R. Z.; Li, Q.; Shen, C. Y. Molecular Dynamics Simulation of Bubble Nucleation in Carbon Dioxide/Hexadecane Solution as an Analog to Foaming of Polyethylene by Super Critical Carbon Dioxide. *J. Plast. Film Sheet* **2011**, *27*, 117−126.
(39) Nagayama, G.; Tsuruta, T.; Cheng, P. Molecular Dynamics Simulation on Bubble Formation in a Nanochannel. *Int. J. Heat Mass Trans.* **2006**, *49*, 4437−4443.
(40) Hess, B.; Kutzner, C.; van der Spoel, D.; Lindahl, E. GROMACS 4: Algorithms for Highly Efficient, Load-balanced, and Scalable Molecular Simulation. *J. Chem. Theory Comput.* **2008**, *4*, 435−447.
(41) Man, V. H.; Li, M. S.; Derreumaux, P.; Nguyen, P. H. Rayleigh-Plesset Equation of the Bubble Stable Cavitation in Water: A Nonequilibrium All-atom Molecular Dynamics Simulation Study. *J. Chem. Phys.* **2018**, *148*, No. 094505.
(42) Case, D. A.; Belfon, K.; Ben-Shalom, I. Y.; Brozell, S. R.; Cerutti, D. S.; Cheatham, T. E., III; Cruzeiro, V. W. D.; Darden, T. A.; Duke, R. E.; Giambasu, G.; Gilson, M. K.; Gohlke, H.; Goetz, A. W.; Harris, R.; Izadi, S.; Izmailov, S. A.; Kasavajhala, K.; Kovalenko, A.; Krasny, R.; Kurtzman, T.; Lee, T. S.; LeGrand, S.; Li, P.; Lin, C.; Liu, J.; Luchko, T.; Luo, R.; Man, V.; Merz, K. M.; Miao, Y.; Mikhailovskii, O.; Monard, G.; Nguyen, H.; Onufriev, A.; Pan, F.; Pantano, S.; Qi, R.; Roe, D. R.; Roitberg, A.; Sagui, C.; Schott-Verdugo, S.; Shen, J.; Simmerling, C. L.; Skrynnikov, N. R.; Smith, J.; Swails, J.; Walker, R. C.; Wang, J.; Wilson, L.; Wolf, R. M.; Wu, X.; Xiong, Y.; Xue, Y.; York, D. M.; Kollman, P. A. *AMBER 2020*; University of California: San Francisco, 2020.
(43) Ono, K.; Condron, M. M.; Teplow, D. B. Structure-neurotoxicity Relationships of Amyloid β-protein Oligomers. *Proc. Natl. Acad. Sci. U. S. A.* **2009**, *106*, 14745−14750.
(44) Jana, M. K.; Cappai, R.; Pham, C. L. L.; Ciccotosto, G. D. Membrane-bound Tetramer and Trimer Aβ Oligomeric Species Correlate with Toxicity Towards Cultured Neurons. *J. Neurochem.* **2016**, *136*, 594−608.
(45) Maier, J. A.; Martinez, C.; Kasavajhala, K.; Wickstrom, L.; Hauser, K. E.; Simmerling, C. ff14SB: Improving the Accuracy of Protein Side Chain and Backbone Parameters from ff99SB. *J. Chem. Theory Comput.* **2015**, *11*, 3696−3713.
(46) Jorgensen, W. L.; Chandrasekhar, J.; Madura, J. D.; Impey, R. W.; Klein, M. L. Comparison of Simple Potential Functions for Simulating Liquid Water. *J. Chem. Phys.* **1983**, *79*, 926−935.
(47) Essmann, U.; Perera, L.; Berkowitz, M. L.; Darden, T.; Lee, H.; Pedersen, L. G. A Smooth Particle Mesh Ewald Method. *J. Chem. Phys.* **1995**, *103*, 8577−8593.
(48) Berendsen, H. J. C.; Postma, J. P. M.; Vangunsteren, W. F.; Dinola, A.; Haak, J. R. Molecular-Dynamics with Coupling to an External Bath. *J. Chem. Phys.* **1984**, *81*, 3684−3690.
(49) Forester, T. R.; Smith, W. SHAKE, Rattle, and Roll: Efficient Constraint Algorithms for Linked Rigid Bodies. *J. Comput. Chem.* **1998**, *19*, 102−111.
(50) Frishman, D.; Argos, P. Knowledge-based Protein Secondary Structure Assignment. *Proteins* **1995**, *23*, 566−579.
(51) Heinig, M.; Frishman, D. STRIDE: a Web Server for Secondary Structure Assignment from Known Atomic Coordinates of Proteins. *Nucleic Acids. Res.* **2004**, *32*, W500−W502.
(52) Roe, D. R.; Cheatham, T. E. PTRAJ and CPPTRAJ: Software for Processing and Analysis of Molecular Dynamics Trajectory Data. *J. Chem. Theory Comput.* **2013**, *9*, 3084−3095.
(53) Sugita, Y.; Okamoto, Y. Replica-exchange Molecular Dynamics Method for Protein Folding. *Chem. Phys. Lett.* **1999**, *314*, 141.
(54) Zhang, T.; Nguyen, P. H.; Nasica-Labouze, J.; Mu, Y.; Derreumaux, P. Folding Atomistic Proteins in Explicit Solvent Using Simulated Tempering. *J. Phys. Chem. B* **2015**, *119*, 6941−6951.
(55) Man, V. H.; He, X.; Derreumaux, P.; Ji, B.; Xie, X.-Q.; Nguyen, P. H.; Wang, J. Effects of All-Atom Molecular Mechanics Force Fields on Amyloid Peptide Assembly: The Case of Aβ16−22 Dimer. *J. Chem. Theory Comput.* **2019**, *15*, 1440−1452.
(56) Man, V. H.; He, X.; Ji, B.; Liu, S.; Xie, X.; Wang, J. Introducing Virtual Oligomerization Inhibition to Identify Potent Inhibitors of Aβ Oligomerization. *J. Chem. Theory Comput.* **2020**, *16*, 3920−3935.
(57) Man, V. H.; He, X.; Gao, J.; Wang, J. Effects of All-Atom Molecular Mechanics Force Fields on Amyloid Peptide Assembly: The Case of the Key Hexapeptide PHF6 of Tau Protein. *J. Chem. Theory Comput.* **2021**, *17*, 6458−6471.
(58) Man, V. H.; Lin, D.; He, X.; Gao, J.; Wang, J. Joint Computational/Cell-Based Oligomerization for Screening Inhibitors of Tau Assembly: A Proof-of-Concept Study. *J. Alzheimers Dis.* **2022**, 1.
(59) Man, V. H.; He, X.; Ji, B.; Liu, S.; Xie, X. Q.; Wang, J. Molecular Mechanism and Kinetics of Amyloid-β42 Aggregate Formation: A Simulation Study. *ACS Chem. Neurosci.* **2019**, *10*, 4643−4658.
(60) Lee, Y.; Choi, Y.; Park, E. J.; Kwon, S.; Kim, H.; Lee, J. Y.; Lee, D. S. Improvement of Glymphatic-lymphatic Drainage of β-amyloid by Focused Ultrasound in Alzheimer's Disease Model. *Sci. Rep.* **2020**, *10*, 16144.
(61) Lord Rayleigh, O. M. F. R. S., VIII. On the Pressure Developed in a Liquid During the Collapse of a Spherical Cavity. *London, Edinburgh, and Dublin Philosophical Magazine and Journal of Science* **1917**, *34*, 94−98.
(62) Plesset, M. W. The Dynamics of Cavitation Bubbles. *J. Appl. Mech.* **1949**, *16*, 277−282.
(63) Dzubiella, J. Interface Dynamics of Microscopic Cavities in Water. *J. Chem. Phys.* **2007**, *126*, 194504.
(64) Tsuge, H. *Micro- and Nanobubbles: Fundamentals and Applications*; Jenny Stanford Publishing, 2014.
(65) Gharat, S. K.; Godiyal, S. C.; Malusare, P. P.; Jadhav, K. R.; Kadam, V. J. Microbubbles Contrast Agents: General Overview as Diagnostics and Therapeutic Agent. *Curr. Drug Targets* **2022**, *23*, 960.
(66) Ogawa, K.; Kato, N.; Yoshida, M.; Hiu, T.; Matsuo, T.; Mizukami, S.; Omata, D.; Suzuki, R.; Maruyama, K.; Mukai, H.; Kawakami, S. Focused Ultrasound/Microbubbles-assisted BBB Opening Enhances LNP-mediated mRNA Delivery to Brain. *J. Controlled Release* **2022**, *348*, 34−41.
(67) Rousou, C.; Schuurmans, C. C. L.; Urtti, A.; Mastrobattista, E.; Storm, G.; Moonen, C.; Kaarniranta, K.; Deckers, R. Ultrasound and Microbubbles for the Treatment of Ocular Diseases: From Preclinical Research towards Clinical Application. *Pharmaceutics* **2021**, *13*, 1782.
(68) Endo-Takahashi, Y.; Negishi, Y. Microbubbles and Nanobubbles with Ultrasound for Systemic Gene Delivery. *Pharmaceutics* **2020**, *12*, 964.
(69) Jose, A. D.; Wu, Z.; Thakur, S. S. A Comprehensive Update of Micro- and Nanobubbles as Theranostics in Oncology. *Eur. J. Pharm. Biopharm.* **2022**, *172*, 123−133.
(70) Shervani-Tabar, M.; Aghdam, A. H.; Khoo, B.; Farhangmehr, V.; Farzaneh, B. Numerical Analysis of a Cavitation Bubble in the Vicinity of an Elastic Membrane. *Fluid Dyn. Res.* **2013**, *45*, No. 055503.
(71) Choubey, A.; Vedadi, M.; Nomura, K.; Kalia, R. K.; Nakano, A.; Vashishta, P. Poration of Lipid Bilayers by Shock-Induced Nanobubble Collapse. *Appl. Phys. Lett.* **2011**, *98*, No. 023701.
(72) Schanz, D.; Metten, B.; Kurz, T.; Lauterborn, W. Molecular Dynamics Simulations of Cavitation Bubble Collapse and Sonoluminescence. *New J. Phys.* **2012**, *14*, 113019.
(73) Nomura, K.; Kalia, R. K.; Nakano, A.; Vashishta, P.; Shekhar, A. Nanobubble Collapse on a Silica Surface in Water: Billion-Atom Reactive Molecular Dynamics Simulations. *Phys. Rev. Lett.* **2013**, *111*, 184503.

(74) Santo, K. P.; Berkowitz, M. L. Shock Wave Induced Collapse of Arrays of Nanobubbles Located Next to a Lipid Membrane: Coarse Grained Computer Simulations. *J. Phys. Chem. B* **2015**, *119*, 8879−8889.
(75) Santo, K. P.; Berkowitz, M. L. Shock Wave Interaction with a Phospholipid Membrane: Coarse-Grained Computer Simulations. *J. Chem. Phys.* **2014**, *140*, No. 054906.
(76) Fu, H.; Comer, J.; Cai, W.; Chipot, C. Sonoporation at Small and Large Length Scales: Effect of Cavitation Bubble Collapse on Membranes. *J. Phys. Chem. Lett.* **2015**, *6*, 413−418.
(77) Man, V. H.; Li, M. S.; Wang, J.; Derreumaux, P.; Nguyen, P. H. Nonequilibrium Atomistic Molecular Dynamics Simulation of Tubular Nanomotor Propelled by Bubble Propulsion. *J. Chem. Phys.* **2019**, *151*, No. 024103.
(78) Man, V. H.; Truong, P. M.; Li, M. S.; Wang, J.; Van-Oanh, N.-T.; Derreumaux, P.; Nguyen, P. H. Molecular Mechanism of the Cell Membrane Pore Formation Induced by Bubble Stable Cavitation. *J. Phys. Chem. B* **2019**, *123*, 71.
(79) Darrow, D. P. Focused Ultrasound for Neuromodulation. *Neurotherapeutics* **2019**, *16*, 88−99.

https://doi.org/10.1021/acs.jcim.2c00764
J. Chem. Inf. Model. 2022, 62, 3885−3895